RSC Advances

PAPER

View Article Online
View Journal | View Issue

Cite this: *RSC Adv.*, 2020, **10**, 28128

Impact of N-substitution on structural, electronic, optical, and vibrational properties of a thiophene–phenylene co-oligomer†

Vasiliy A. Trukhanov, *[ab] Dmitry I. Dominskiy, [a] Olga D. Parashchuk, [a] Elizaveta V. Feldman,[a] Nikolay M. Surin, [c] Evgeniya A. Svidchenko, [c] Maxim S. Skorotetcky,[c] Oleg V. Borshchev, [c] Dmitry Yu. Paraschuk [a] and Andrey Yu. Sosorev [ab]

Properties of the organic semiconductors can be finely tuned *via* changes in their molecular structure. However, the relationship between the molecular structure, molecular packing, and (opto)electronic properties of the organic semiconductors to guide their smart design remains elusive. In this study, we address computationally and experimentally the impact of subtle modification of a thiophene–phenylene co-oligomer CF_3-PTTP-CF_3 on the molecular properties, crystal structure, charge transport, and optoelectronic properties. This modification consists in the substitution of two C–H atom pairs by N atoms in the thiophene units and hence converting them to thiazole units. A dramatic effect of the N-substitution on the crystal structure—the crossover from the herringbone packing motif to π-stacking—is attributed to significant changes in the molecular electrostatic potential. The changes in the molecular and crystal structure resulting from the N-substitution clearly reveal themselves in the Raman spectra. The increase of the calculated electron mobility in the corresponding crystals as a result of the N-substitution is rationalized in terms of the changes in the molecular and crystal structure. The charge transport, electroluminescence, and photoelectric properties are compared in thin-film organic field-effect transistors based on CF_3-PTTP-CF_3 and its N-substituted counterpart. An intriguing similarity between the effects of N-substitution in the thiophene rings and fluorination of the thiophene–phenylene oligomer is revealed, which is probably associated with a more general effect of electronegative substitution. The obtained results are anticipated to facilitate the rational design of organic semiconductors.

Received 14th April 2020
Accepted 17th July 2020

DOI: 10.1039/d0ra03343j

rsc.li/rsc-advances

1. Introduction

Organic semiconductors (OSs) with high charge-carrier mobility and efficient luminescence are necessary for organic optoelectronic devices, *e.g.*, organic light-emitting diodes,[1] organic light-emitting transistors,[2] and electrically pumped solid-state organic lasers.[3] These features are luckily combined in conjugated oligomers and co-oligomers, which makes these compounds promising candidates for using in organic optoelectronics.[4] Some (co)oligomers combine strong light absorption in UV-vis spectral region with decent charge-carrier mobility so that the photoelectric effect can be efficient making them useful for development of novel organic phototransistors.[5] Moreover, synthetic flexibility of the conjugated (co)oligomers enables their prompt chemical modification for fine-tuning of the electronic and optical properties.

Although a plenty of conjugated (co-)oligomers were synthesized, the structure–property relationships for their rational design remain poorly understood. Specifically, it is well known that very small changes in the chemical structure can dramatically affect the crystal packing and physico-chemical properties of the OSs (see, *e.g.*, ref. 6–9). For instance, substitution of hydrogen atoms with fluorine ones (fluorination) typically facilitates a crossover from the herringbone packing commonly observed in OS crystals to the π-stacking motif, which is considered more favorable for charge transport.[7–15] However, the effect of fluorination on the optoelectronic properties is not always positive: in several cases, fluorination results in a decrease in photoluminescence quantum yield (PLQY) and absorption,[9] and extensive fluorination can deteriorate the charge mobility.[7,8,16] Moreover, in exotic cases fluorination induces the opposite crossover in the crystal structure—from the

[a]*Faculty of Physics & International Laser Centre of Lomonosov Moscow State University, Leninskiye Gory 1/62, Moscow 119991, Russia. E-mail: trukhanov@physics.msu.ru*

[b]*Institute of Spectroscopy of the Russian Academy of Sciences, Fizicheskaya St. 5, Troitsk, Moscow 108840, Russia*

[c]*Enikolopov Institute of Synthetic Polymeric Materials of Russian Academy of Sciences, Profsoyuznaya St. 70, Moscow 117393, Russia*

† Electronic supplementary information (ESI) available. See DOI: 10.1039/d0ra03343j

π-stacking to herringbone motif.[17–19] Thus, it is important to predict whether certain changes in the molecular (chemical) structure will be favorable or detrimental for optoelectronic applications. This prediction could be based on general "molecular structure – crystal structure – (opto)electronic properties" relationships, which are now in the focus of the material science.

Very recently, two ways of tailoring the optoelectronic properties of the thiophene–phenylene co-oligomers—addition of terminal groups[20] and fluorination[16]—have been investigated in detail. However, there is another tool for tuning the OS properties—the heteroatomic substitution in the very conjugated core. This type of modification can have a stronger impact on the optoelectronic properties because it is directly related to the distribution of the electron density at the frontier molecular orbitals, which determine the optoelectronic properties. Among heteroatoms, nitrogen attracts a particular attention. Introduction of nitrogen into the conjugated core of the OSs (intra-ring N-substitution) significantly decreases the energies of the frontier orbitals and can change the conductivity type from the hole to electron one.[21,22] An interesting material among the N-substituted conjugated co-oligomers is 2,2′bis[4-(trifluoromethyl)phenyl]-5,5′-bi-1,3-thiazole (**CF_3-PTzTzP-CF_3**) (see Fig. 1 for chemical structure). According to ref. 23 and 24, the electron mobility, μ_e, in **CF_3-PTzTzP-CF_3** exceeds that in **CF_3-PTTP-CF_3** (its counterpart without nitrogen) by an order of magnitude. The μ_e value higher than 1 $cm^2 V^{-1} s^{-1}$ reported in ref. 23 for **CF_3-PTzTzP-CF_3** is very unusual for oligomers and is usually observed for fused aromatics,[25] which generally show more favorable molecular packing with the stronger electronic interaction between the molecules. The earlier computational studies reproduced the reported difference in μ_e in the two aforementioned oligomers.[26,27] The difference was tentatively assigned to the dramatic difference in the crystal structure for the two compounds: while **CF_3-PTTP-CF_3** packs in a herringbone motif typical for OSs, **CF_3-PTzTzP-CF_3** shows π-stacking, which is considered beneficial for charge transport.[28,29] But what is the mechanism underlying the change of the crystal packing for these compounds? Is this mechanism specific for these compounds or general for conjugated oligomers? And does the N-substitution affect optical properties of conjugated (co)oligomers? These questions have not been answered yet.

In this study, we address computationally and experimentally the structure–property relationships underlying the difference in the properties between **CF_3-PTTP-CF_3** and **CF_3-PTzTzP-CF_3**. Specifically, we focus on the relationships between the molecular structure and properties, the molecular and crystal structures, and impact of the molecular/crystal structure on the charge-carrier mobility. First, density functional theory (DFT) calculations along with absorption, photoluminescence (PL) and Raman spectroscopies are applied to compare the electronic, optical, and vibrational properties of the isolated molecules. Then, the physics underlying the difference in the crystal packing is unraveled, and the impact of this difference on charge mobility is modeled. To explore the potential of both oligomers for (opto)electronic devices, organic field-effect transistors (OFETs) with thin-film active layers of both oligomers are fabricated and studied, and they demonstrate electroluminescence and a photoelectric effect. The observed impact of the intra-ring N-substitution on the structural, electronic, vibrational, optical and charge-transport properties is compared with the effect of fluorination recently addressed in ref. 16, and intriguing similarities possibly related to general relationships between the molecular structure, crystal structure and (opto)electronic properties are revealed.

2. Methods

2.1. Calculations

Density functional theory (DFT) and time-dependent DFT (TDDFT) calculations were performed using GAMESS package[30,31] at B3LYP/6-31G(d,p) level. The reorganization energy for electron transport, λ, was approximated by its inner-sphere part, which is typically considered much larger than the outer-sphere part for OSs.[32] The λ values were calculated according to the common adiabatic potentials (4-point) scheme[33] from the energies of the molecule in the following four states: the neutral state in its optimized geometry (E_N), the neutral state in the optimized geometry of the negatively charged state (E_{N^*}), the negatively charged state in its optimized geometry (E_C), and the negatively charged state in the geometry of the neutral state (E_{C^*}): $\lambda = (E_{N^*} - E_N) + (E_{C^*} - E_C)$. Electron transfer integrals J_i were calculated using a home-written code based on the dimer projection method (DIPRO).[34–36] Electrostatic potential was visualized using JMol package,[37] and molecular orbitals were visualized using Chemcraft.[38] Conjugated lengths were calculated as suggested in ref. 16. Hirshfeld surface analysis and energy framework calculations were performed at B3LYP/6-31g(d,p) level in CrystalExplorer17.5 software.[39,40]

2.2. Sample preparation

The **CF_3-PTTP-CF_3** was synthesized according to previous work[41] and **CF_3-PTzTzP-CF_3** (97% purity) was purchased in Sigma-Aldrich.

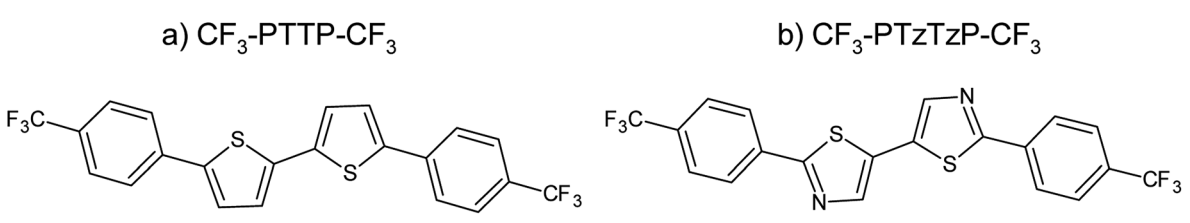

Fig. 1 Chemical structure of the compounds studied.

2.3. Raman spectroscopy

For Raman measurements, powders of **CF_3-PTTP-CF_3** and **CF_3-PTzTzP-CF_3** were compressed into tablets. Raman measurements in the spectral range 10–1800 cm^{-1} were conducted using a Raman microscope (inVia, Renishaw) with a 50× objective lens (Leica DM 2500 M, NA = 0.75). The excitation wavelength was 633 nm provided by a He–Ne laser (RL633, Renishaw) with the maximum power of 17 mW. Low-frequency (LF) measurements were conducted using a NExT monochromator, high-frequency (HF) measurements were performed with a 633 nm edge filter. The LF and HF measurements were performed separately, and then the LF and HF spectra were merged. The accumulation time and the pump intensity were selected to increase the signal-to-noise ratio and minimize photodegradation. All spectra were measured in several points of the sample and then averaged to reduce the anisotropy effect on the Raman spectra.

2.4. Absorption and photoluminescence

The absorption spectra were recorded on a Shimadzu UV-2501PC spectrophotometer in a 10 mm-thick photometric quartz cuvette using tetrahydrofuran (THF) solutions with the oligomer concentrations of 10^{-5} M. Photoluminescence spectra (PL) in solution were recorded by using of a scanning spectrofluorimeter ALS01M operating in the single-photon-counting mode.[42] The PL measurements were carried out in the 90°-geometry for several optical densities of the sample in the range of 0.06–0.12 absorbance units by using a 10 mm-thick cuvette. The PL quantum yield (QY) was measured by comparing the integral PL intensity of 10^{-6} M diluted solutions in THF with the integral PL intensity of the standard as described elsewhere.[43] As a PLQY standard, solution of 1,4-bis(5-phenyloxazol-2-yl) benzene (POPOP) in cyclohexane (PLQY = 0.93) was used.

2.5. OFET fabrication and characterization

OFET samples were fabricated in the top-contact bottom-gate architecture on silicon substrates with 200 nm-thick thermally grown oxide (SiO_2) dielectric layer covered with a poly(-methylmethacrylate) (PMMA) or hexamethyldisilazane (HMDS) layer. Si/SiO_2 substrates were treated as described in ESI, Section S6.† Thin-film (polycrystalline) OFET active layers of the **CF_3-PTTP-CF_3** and **CF_3-PTzTzP-CF_3** were thermally evaporated in a vacuum chamber at a pressure in the range 3.3×10^{-6}–4.7×10^{-6} mbar with the evaporation rate in the range of 1.0–2.5 Å s^{-1}, the thickness was 50 nm according to a thickness monitor (TM400, Maxtek). On the substrates with the deposited active layer the source and drain electrodes were thermally evaporated in vacuum through Ossila shadow masks. As a result, 20 devices per substrate with different channel lengths from 10 to 30 μm with a step of 5 μm and the channel width of 1 mm were formed. The two types of source/drain electrodes were used: calcium (Ca) for electron injection and bilayer of molybdenum oxide and silver (MoO_3/Ag) for hole injection. Output and transfer characteristics of OFET samples were measured for all devices using a probe station (Printeltech 100) and a source measure unit (Keithley 2636A). The transfer characteristics were measured in both forward and backward directions of the voltage sweep to reveal hysteresis in the charge carrier mobility. The electron mobility (μ_e) values, as well as threshold voltage (V_{th}), in the linear and saturation regimes were calculated by approximation of the measured transfer characteristics to the common Shockley equations. The voltage ranges of approximation were chosen to achieve the best fit, wherein the fitting ranges were not less than 2/3 of the range of measurement in the corresponding regime. The mobility and V_{th} data were averaged over 20 devices and both directions of the voltage sweep for each OFET substrate. Light emission was captured using a microscope equipped with a CCD-camera (Infinity 3, Luminera) at an exposition time of 60 s during transfer characteristics measurement. The relative electroluminescence intensity was calculated as a sum of intensities of pixels belonging to the channel area in a captured light-emission image. The study the photoelectric effect in the OFET samples, their transfer characteristics under white-LED light illumination with an intensity of 100 mW cm^{-2} were measured. The thicknesses of OFET active layers and their surface profiles were measured with an atomic-force microscope (AFM) Ntegra Spectra (NT-MDT). Other details of the OFET fabrication and characterization are given in ESI.†

3. Results and discussion

3.1. Molecular structure and properties

3.1.1. DFT calculations. Fig. 2 presents the equilibrium geometries and patterns of the frontier molecular orbitals: the highest occupied molecular orbital (HOMO) and the lowest unoccupied molecular orbital (LUMO). From this figure it follows that although the phenylene rings are twisted in **CF_3-PTTP-CF_3** with respect to the thiophene ones, in **CF_3-PTzTzP-CF_3** they are in the same plane with thiophene ones. This is in line with the results of ref. 26 and 44. The torsion of the phenylene rings with respect to the thiophene ones, which is observed in **CF_3-PTTP-CF_3**, is explained by the repulsion between positively charged hydrogen atoms of the phenylene and thiophene rings.[33,45] On the contrary, in **CF_3-PTzTzP-CF_3**, the substitution of thiophene rings with thiazole ones eliminates this repulsion because of the absence of the corresponding hydrogen atom. Moreover, Fig. 2(e and f) indicates that nitrogen atoms in the thiazole rings bear a negative electrostatic potential attracting the positively-charged hydrogen cores of the phenylene rings, further stimulating the molecular planarization. Importantly, the emergence of the areas of strongly negative charge on the conjugated core upon the intra-ring N-substitution significantly affects crystal packing as shown below.

The HOMO and LUMO energies are presented in Table 1. The N-substitution results in a decrease of the HOMO and LUMO energies of **CF_3-PTTP-CF_3** by 0.44 and 0.38 eV, respectively. The HOMO–LUMO gap, E_{HL}, and optical gap, E_g, slightly widen with substitution, and the oscillator strength slightly decreases. These effects can be attributed to the slight decrease

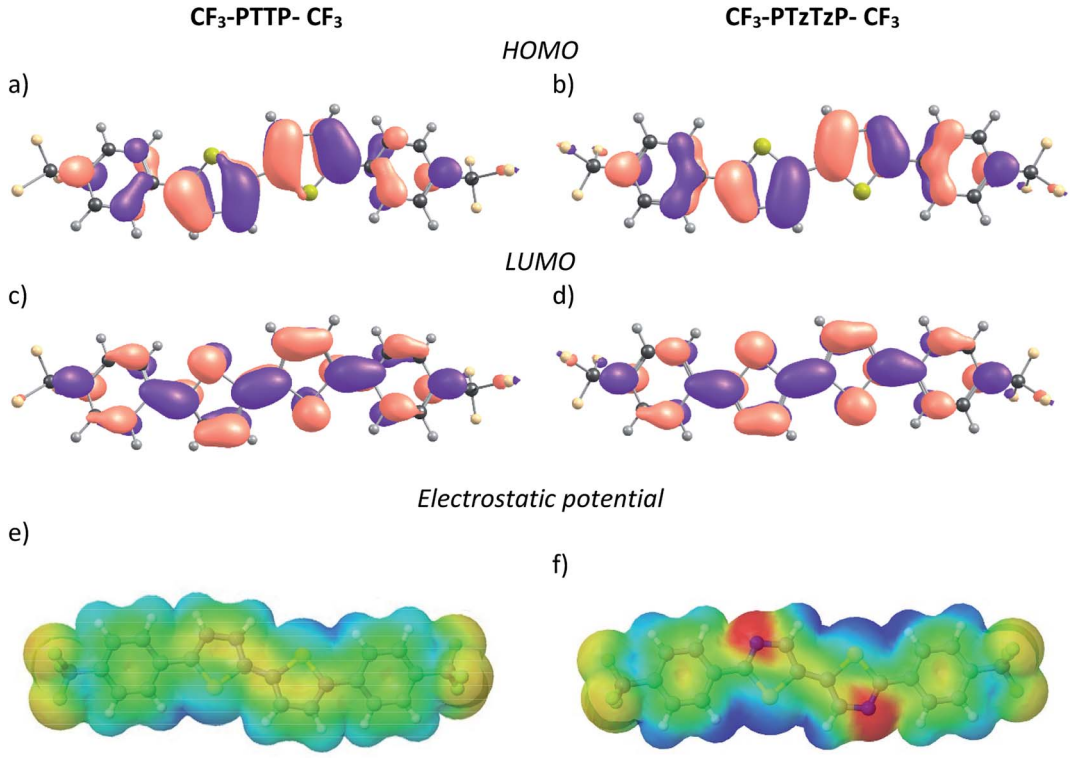

Fig. 2 Equilibrium geometries, HOMO (a and b) and LUMO (c and d) patterns, and electrostatic potential maps (e and f) for the compounds studied.

in the conjugation length from 6.65 Å for **CF_3-PTTP-CF_3** to 6.59 Å for **CF_3-PTzTzP-CF_3**.

3.1.2. Absorption and photoluminescence in solution. Fig. 3 presents absorption and photoluminescence spectra in THF solutions for both oligomers, where molecules are separated by the solvent so that optical properties of the individual molecules are probed. This figure clearly shows that the N-substitution results in a blueshift of both the absorption and photoluminescence (PL) spectra, which is in line with our computational results (see Table 1). PL quantum yield somewhat increases from 17% to 25% as a result of the N-substitution.

3.1.3. High-frequency Raman spectra. Raman spectroscopy provides important information about vibrational properties of the materials reporting on the molecular and crystal structure. Fig. 4 collates Raman spectra of the polycrystalline powders of the two oligomers. As follows from the figure the high-frequency Raman spectra (ω > 200 cm^{-1}), which are associated with intramolecular vibrations,[46,47] are very similar for **CF_3-PTTP-CF_3** and **CF_3-PTzTzP-CF_3**. Specifically, all the most intensive bands are located in the range 1000–1700 cm^{-1}. The positions of bands at frequencies at ~1411, 1518, 1615 cm^{-1} are similar for both oligomers. For **CF_3-PTTP-CF_3**, these modes were previously suggested to possess a dominant contribution from vibrations of the phenylene rings,[20] and hence it is natural that they are weakly affected by the chemical modification of the thiophene

Table 1 The HOMO and LUMO energies, HOMO–LUMO gaps, optical gap, and oscillator strength, *f*, for the compounds studied

	HOMO	LUMO	E_{HL}	E_g	*f*
CF_3-PTTP-CF_3	−5.45	−2.13	3.32	3.055	1.34
CF_3-PTzTzP-CF_3	−5.89	−2.51	3.39	3.091	1.28

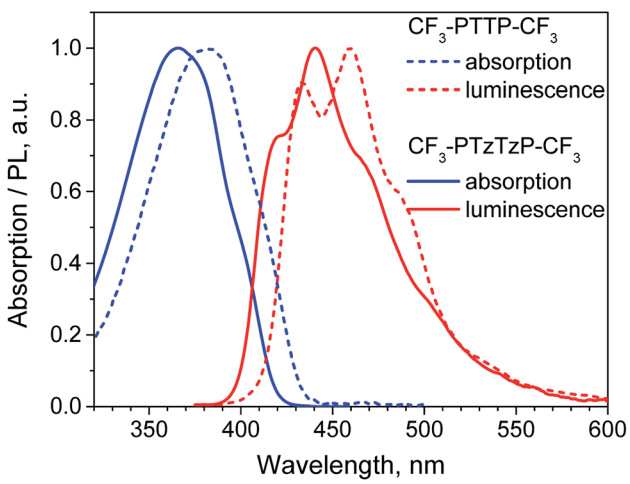

Fig. 3 Absorption and photoluminescence spectra of CF_3-PTTP-CF_3 and CF_3-PTzTzP-CF_3 in THF solution.

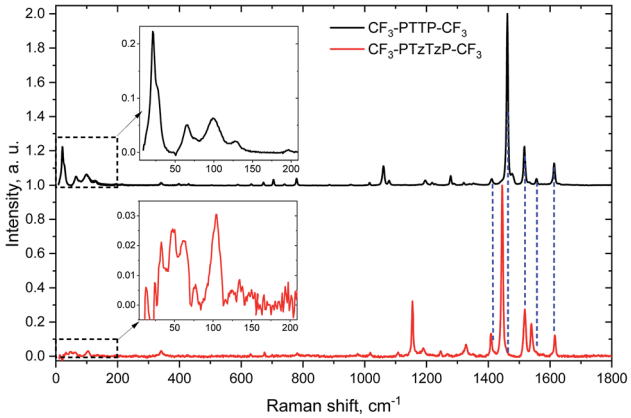

Fig. 4 Experimental Raman spectra of polycrystalline powders of CF_3-PTTP-CF_3 (black) and CF_3-PTZTZP-CF_3 (red) normalized to the maximal intensity in the high-frequency range. Insets show the low-frequency (LF) range. Dashed blue lines indicate the positions of selected Raman bands of CF_3-PTTP-CF_3.

rings. On the contrary, the modes observed at 1463, 1555 cm^{-1} in **CF_3-PTTP-CF_3** are redshifted in **CF_3-PTZTZP-CF_3**. These bands have a dominant contribution from the vibrations of the thiophene rings.[20] Thus, the N-substitution in the thiophene rings results in a frequency shift of the mentioned bands probably because of higher mass of nitrogen as compared to carbon. The low-frequency (LF) range (<200 cm^{-1}) of the Raman spectra is discussed in the next section.

3.2. Molecular and crystal structures

3.2.1. Crystal structure. To rationalize the impact of N-substitution on crystal packing, we compared crystal structures of **CF_3-PTTP-CF_3** and **CF_3-PTZTZP-CF_3** reported by Ando *et al.* (CCDC numbers 1427491 and 291639, respectively),[48,49] and analyzed them using the energy framework and Hirshfeld approaches. These structures are sketched in Fig. 5 showing that **CF_3-PTTP-CF_3** has a clear layered structure: the molecular layers correspond to the *ab* plane (nearly normal to the long molecular axes) and are separated by terminal CF_3 groups. Within the layers, molecules are arranged in the herringbone packing motif without face-to-face overlap (Fig. 5(b)). As follows from the energy framework analysis (Fig. 6(a) and ESI, Section S2†), the strongest interactions are observed within the layers. In the **CF_3-PTZTZP-CF_3** crystal, the layer structure changes: the strongest (intralayer) interactions here are in the planes containing the long molecular axes and direction(s) of π-stacking (see Fig. 5(c) and 6(b)). The packing motif transforms into brickwall packing with two-dimensional π-stacking (Fig. 5(d)).[50,51] Surprisingly, the unit cell parameters are altered moderately (see Fig. 5): the crystal system for **CF_3-PTZTZP-CF_3** stays monoclinic as for **CF_3-PTTP-CF_3**, and there are also two molecules in the unit cell ($Z = 2$).

3.2.2. Hirshfeld analysis. Hirshfeld surface analysis[52] of **CF_3-PTTP-CF_3** and **CF_3-PTZTZP-CF_3** crystal structures was carried out to reveal the intermolecular interactions governing the packing motifs in these crystals. The Hirshfeld surface defines the space occupied by a molecule in the crystal: inside this surface, the electron density from the given molecule is larger than that from the others.[53] Fig. 7 displays the Hirshfeld surfaces for the two crystals mapped with two important properties: curvedness (C) and electrostatic potential (ESP); see ESI, Section S1,† and ref. 52 and 54 for their definitions. The curvedness maps shown in Fig. 7(a) can be used to analyze the molecular packing motifs.[52] Specifically, the π-stacking arrangement of the molecules can be identified by relatively large green flat regions (see also ESI, Section 1†) at this map. The map for **CF_3-PTTP-CF_3** has no such regions, which indicates a herringbone packing.[52] On the contrary, the map for **CF_3-PTZTZP-CF_3** shows two extended green regions at its face, which reveal π-stacking of **CF_3-PTZTZP-CF_3** with two adjacent molecules per one molecule face (*i.e.*, two-dimensional π-stacking). The directions of π-stacking correspond to the directions of the strongest intermolecular interactions (see Fig. 6(b)).

Fig. 7(b) shows that the electrostatic potential of **CF_3-PTZTZP-CF_3** differs from that of **CF_3-PTTP-CF_3**: whereas the thiophene rings in **CF_3-PTTP-CF_3** generally have the electronegative center and the electropositive periphery (hydrogen atoms), the nitrogen atoms in thiazole rings of **CF_3-PTZTZP-CF_3** pull out the electron density making the rest of the ring electropositive. This is in line with our calculations for isolated molecules (see Fig. 2(e and f)). As a result, in the **CF_3-PTZTZP-CF_3** crystal, the thiazole rings always pack next to the phenylene rings, resulting in the ESP complementarity (Fig. S3†).[55] Thus, we suggest that the abovementioned two-dimensional π-stacking observed in the **CF_3-PTZTZP-CF_3** crystal is partially induced by the face-to-face electrostatic interactions between the N-substituted and non-substituted aromatic rings. In addition, the emergence of strongly electronegative areas at the edges of the molecule facilitates edge-to-edge interactions in the **CF_3-PTZTZP-CF_3** crystal, which is indicated by formation of close edge-to-edge contacts (see Fig. S1†). As a result, we attribute the observed crossover from the herringbone packing in **CF_3-PTTP-CF_3** to π-stacking in **CF_3-PTZTZP-CF_3** to the fact that the face-to-face and edge-to-edge interactions (facilitating π-stacking) in the latter crystal overwhelm the edge-to-face interactions (facilitating herringbone packing).

Fig. 8 depicts the contributions of various atoms types to the intermolecular contacts in the crystals studied; the details of the analysis of the molecular contacts are given in ESI, Section S1.† As follows from this figure, the major contribution for **CF_3-PTTP-CF_3** comes from C···H (typical for herringbone packing), F···F (because of the layered structure) and F···H contacts (because of electrostatic attraction of these atoms). For **CF_3-PTZTZP-CF_3**, the main contribution also comes from F···H and C···H contacts; however, the percentage of the former contacts increases significantly as a result of the interpenetration of the molecules into adjacent layers, while the percentage of the latter contacts significantly decreases as a result of the disappearance of the herringbone structure. Importantly, for **CF_3-PTTP-CF_3**, the percentage of the "conducting" contacts, *i.e.*, the contacts between the atoms bearing large HOMO and/or LUMO electron density (see Fig. 2), is just 4% and stems from S–C and S–S contacts. On the contrary, for **CF_3-PTZTZP-CF_3**, this percentage increases to 13% and stems from C–C and N–C contacts. The increase in the "conducting" contacts number (C···C, S···C, S···

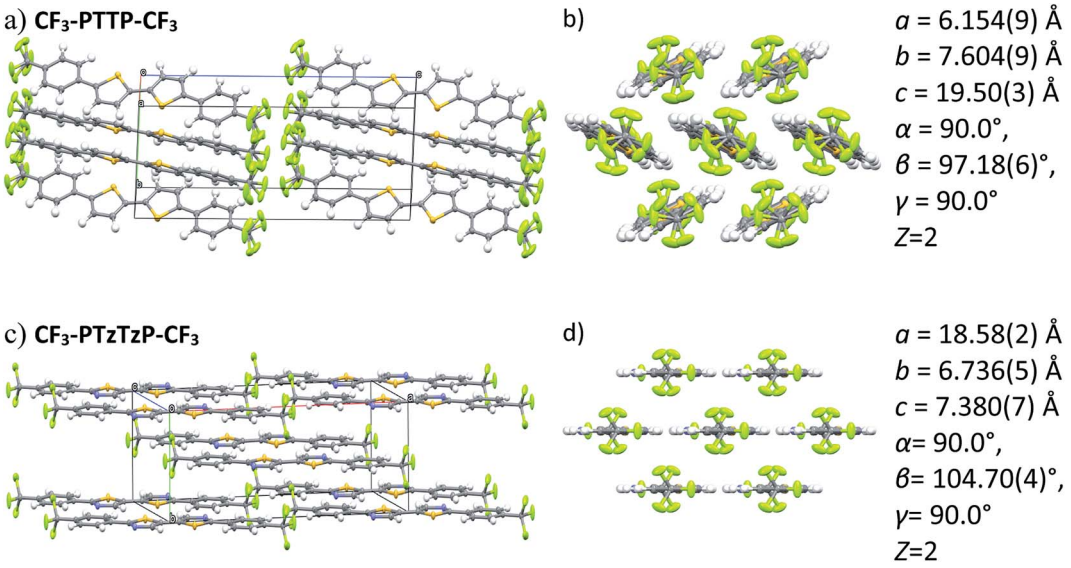

Fig. 5 Crystal structures (two projections) for CF_3-PTTP-CF_3 (a and b) and CF_3-PTzTzP-CF_3 (c and d) and the corresponding unit cell parameters.

S, N···C, N···S, N···N) with the N-substitution should be attributed to the change in the packing motif from the herringbone one (CF_3-PTTP-CF_3) to brickwall packing (CF_3-PTzTzP-CF_3), in line with Fig. 4(a) and ES1.† This increase is favorable for charge transport as discussed below.

3.2.3. Low-frequency Raman spectra. As mentioned above, LF Raman spectra are sensitive to the crystal structure and hence can monitor its changes.[46,56,57] Fig. 4 shows that the LF bands for CF_3-PTzTzP-CF_3 have a considerably lower intensity than those for CF_3-PTTP-CF_3. It was previously suggested that the LF Raman spectra are related to vibrational modulation of the charge transport integrals and the molecular polarizability: the more intense the LF Raman signal, the stronger this modulation.[46,58] Thus, the decrease in the LF Raman intensity can be attributed to a weaker impact of the corresponding vibrations on the charge transfer integrals between the molecules, *i.e.*, the lower dynamic disorder. The latter is favorable for charge transport.[59,60] The other factors affecting the charge mobility are analyzed in the next section.

3.3. Charge transport

3.3.1. Calculations. To address the impact of the molecular structure change in the crystal structure on the charge-carrier (electron and hole) mobility, μ, we calculated the μ values within the widely used hopping model based on the Marcus formula for the charge-transfer rate:[61]

$$k = \frac{2\pi}{\hbar} J^2 \left(\frac{1}{4\pi\lambda k_B T}\right)^{1/2} \exp\left(-\frac{(\Delta E - \lambda)^2}{4\pi\lambda k_B T}\right), \quad (1)$$

where ħ is the reduced Planck constant, k_B is the Boltzmann constant, T is the absolute temperature, J is the charge transfer integral describing the electronic coupling between the sites, λ is the reorganization energy of the site that describes the local electron–phonon interaction, and ΔE is the electron energy difference between the initial and final sites ($\Delta E = 0$ if the molecules are identical). Then, the charge-carrier mobility was estimated using the common Einstein–Smoluchowski relation:[32]

$$\mu = \frac{eD}{kT} = \frac{e}{6kT} \sum_i k_i r_i^2 p_i, \quad (2)$$

where D is the charge-carrier diffusion coefficient, r_i is the distance between the adjacent molecules along the i-th transport direction, and $p_i = \frac{k_i}{\sum_j k_j}$ is the probability of the charge carrier to move in this direction. As follows from eqn (1) and (2),

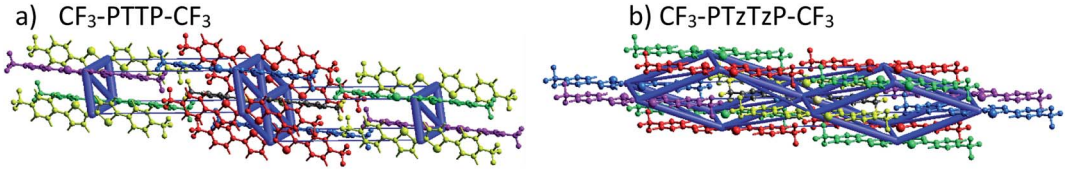

Fig. 6 Graphical representation of the total interaction energy in blue on panel in CF_3-PTTP-CF_3 (a) and CF_3-PTzTzP-CF_3 (b) crystals. The cylinders link molecular centroids, and their thickness is proportional to the magnitude of the energy; for clarity, the pairwise energies with magnitudes less than 5 kJ mol^{-1} are not shown. Details are given in Table S1 and S2.†.

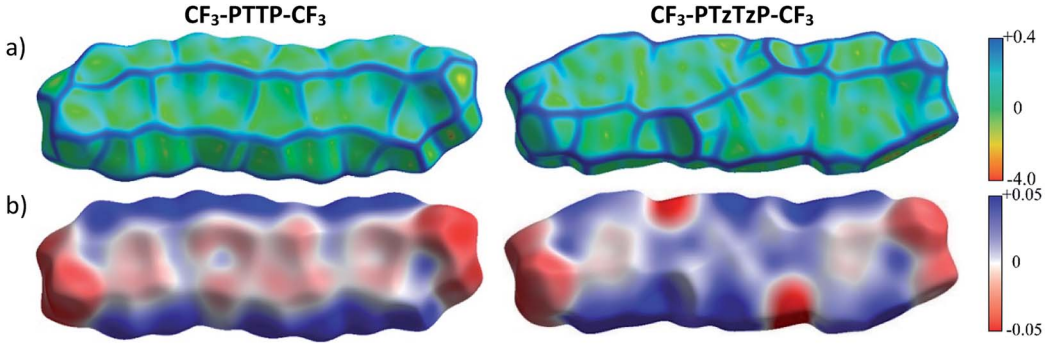

Fig. 7 Hirshfeld surfaces of CF_3-PTTP-CF_3 and CF_3-PTzTzP-CF_3 mapped with curvature C (a) and ESP (±65.6 kJ mol^{-1} per unit charge) (b).

the higher the J_i and r_i values and the lower the λ values, the larger the μ values.

The calculated reorganization energy for electron transfer, λ, is 420 meV for **CF_3-PTTP-CF_3** and 320 meV for **CF_3-PTzTzP-CF_3**; these values correspond well with the results of previous works.[26,44] Thus, the N-substitution significantly decreases λ, and this is beneficial for charge transport. The decrease of λ in **CF_3-PTzTzP-CF_3** can be attributed the elimination of repulsion between the hydrogen atoms of the thiophene and phenylene rings (which torsionally distorts the conjugated core in **CF_3-PTTP-CF_3**) leading to planarization of the conjugated core and restriction of torsional degrees of freedom, which significantly contribute to the reorganization energy of thiohene-phenylene co-oligomers.[62]

Fig. 9 presents the charge transfer integrals, J, for the two crystals. In **CF_3-PTTP-CF_3**, there is a single direction with large J ~ 80 meV; there are also two directions with J ~ 20 meV. For **CF_3-PTzTzP-CF_3**, there are two directions with J ~ 70 meV and one direction with J ~ 20 meV. Since it is frequently assumed that the charge transport is efficient if J exceeds the energy of thermal fluctuations (25 meV at room temperature), in the latter crystal, the charge transport is quasi-two-dimensional, whereas in the former it is quasi-one-dimensional. The increase in the charge transport dimensionality can be favorable for μ.[63] Moreover, in **CF_3-PTzTzP-CF_3**, high J are observed for directions with large r_i, which is also beneficial for charge transport (see eqn (2) and Table S3†). Noteworthily, in both crystals, the efficient charge transport should occur exclusively within the layers (see Fig. 5 and 6; note that layered structure differs for the two crystals). This is reasonable since intralayer intermolecular interactions are much stronger than the interlayer ones (see Fig. S5†).

The μ_e values calculated using eqn (1) with the above-mentioned J and λ are 0.065 cm^2 V^{-1} s^{-1} for **CF_3-PTTP-CF_3** and 0.43 cm^2 V^{-1} s^{-1} for **CF_3-PTzTzP-CF_3**. Thus, the N-substitution results in about one order of magnitude increase in μ_e, in line with earlier calculations[27] and experimental[23,24] data. The hole mobility increases as well from 0.0047 cm^2 V^{-1} s^{-1} in **CF_3-PTTP-CF_3** to 0.43 cm^2 V^{-1} s^{-1} in **CF_3-PTzTzP-CF_3**; however, the experimental data for hole transport in these materials are unavailable. The μ_e increase with the N-substitution can be attributed to the two factors: decrease in λ and increase in the J_i values for the directions with large r_i.

3.3.2. Experiment. To compare the charge-transport properties in **CF_3-PTTP-CF_3** and **CF_3-PTzTzP-CF_3**, thin-film OFETs were fabricated in the closest possible conditions for both oligomers. The devices showed only electron transport in line with the earlier studies on **CF_3-PTTP-CF_3** and **CF_3-PTzTzP-CF_3** thin-film OFETs.[23,24] Fig. 10 demonstrates typical transfer characteristics for the OFETs prepared with HMDS (panels a, b) and PMMA (panels c, d) interlayers. The corresponding output characteristics and the electron mobility, μ_e, *vs.* the threshold voltage, V_{th}, diagrams for all fabricated devices are given in Fig. S10 and S11,† correspondingly. Fig. 11 shows histograms

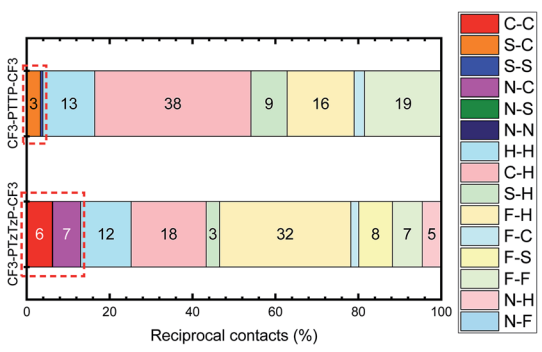

Fig. 8 Distribution of intermolecular contacts for CF_3-PTTP-CF_3 and CF_3-PTzTzP-CF_3 arranged by molecules on the basis of Hirshfeld surface analysis. "Conducting" contacts (see details in the text) are highlighted with the dashed frames.

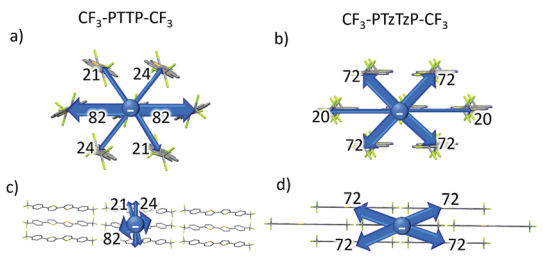

Fig. 9 Charge transfer integrals, J, for CF_3-PTTP-CF_3 and CF_3-PTzTzP-CF_3; the J values are labeled. The thickness of the arrows illustrates the J magnitude.

with the maximal and average values of μ_e and the average values of V_{th} for all the prepared OFETs. The maximum μ_e values among the all devices were in the range 0.03–0.07 $cm^2 V^{-1} s^{-1}$. In the OFETs with HMDS layers, the electron mobility for the N-substituted oligomer is about 1.5–2 times higher than that for its non-substituted counterpart. The higher μ_e values in the N-substituted oligomer are in line with our computational results (see above) and the earlier experimental studies.[23,24] Nevertheless, the analogous devices with PMMA layers showed the somewhat higher but very close μ_e values for both oligomers. The higher μ_e values for these devices correlate with the lower average roughness of the active layer surface deposited on PMMA as compared to HMDS (see the AFM data in Fig. S15†). Accordingly, the film morphology on PMMA for both oligomers is more favorable for charge transport than that on HMDS. Note that the dispersion in the V_{th} values (Fig. 11) is considerably lower for the OFETs with PMMA layers, and, therefore, the data on the devices with PMMA layers are more conclusive for comparison of the charge-transport properties of **CF_3-PTTP-CF_3** and **CF_3-PTzTzP-CF_3**. Thus, we do not observe a clear difference in charge transport in **CF_3-PTTP-CF_3** and **CF_3-PTzTzP-CF_3** thin films. Possibly, the polycrystalline structure of the thin films studied masks the difference in charge transport predicted by our calculations presented above. To get rid of possible effects of the polycrystallinity, single-crystal OFETs should be fabricated and studied; however, this is a subject of our further studies.

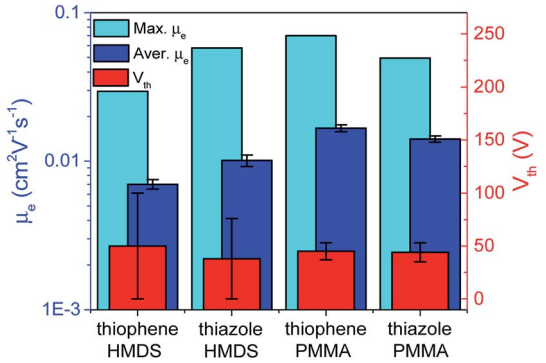

Fig. 11 Maximal and average electron mobilities and average threshold voltages for all prepared devices with HMDS or PMMA layers based on thiophene-containing (CF_3-PTTP-CF_3) and thiazole-containing (CF_3-PTzTzP-CF_3) oligomers.

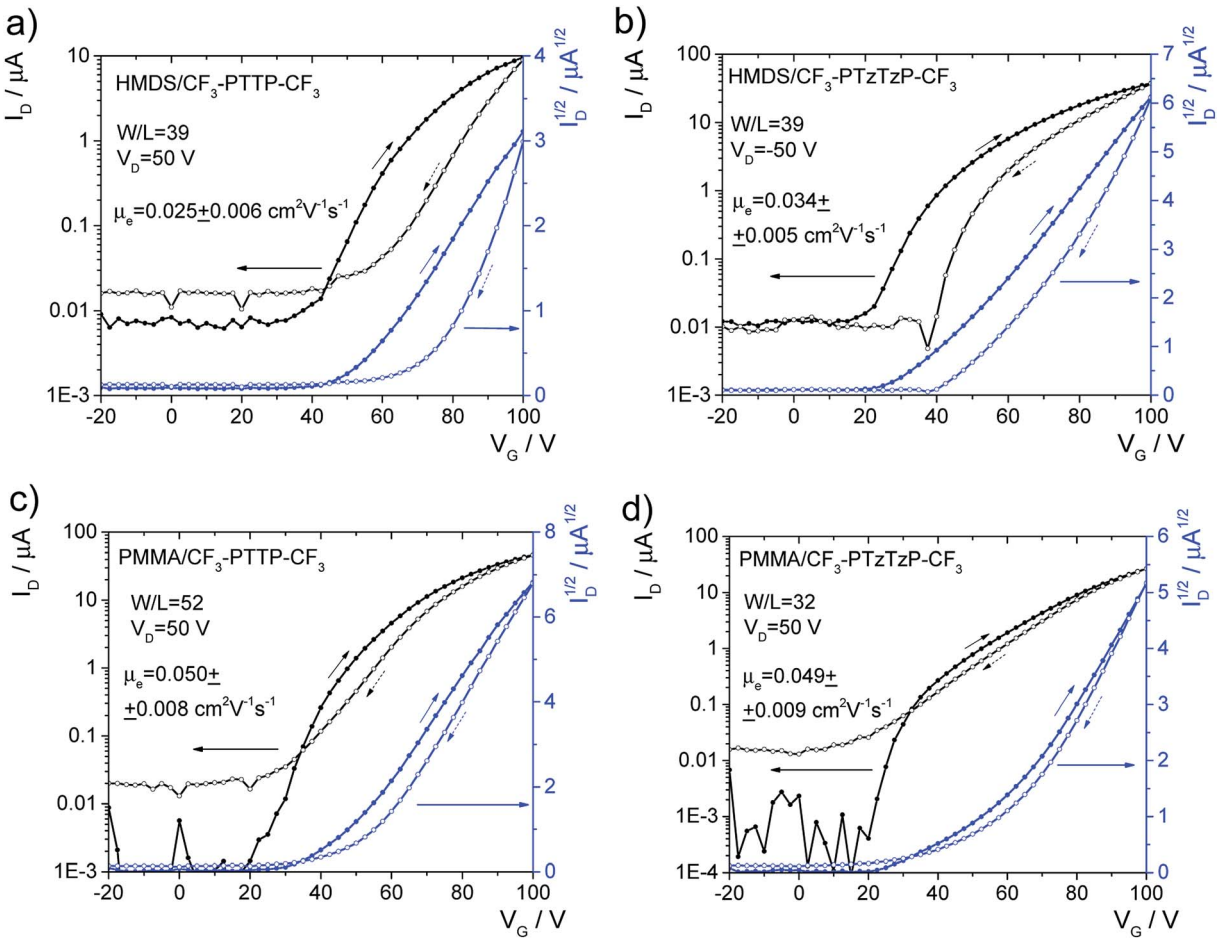

Fig. 10 Typical transfer characteristics of OFETs based on CF_3-PTTP-CF_3 (a and c) and CF_3-PTzTzP-CF_3 (b and d) with HMDS (a and b) and PMMA (c and d) dielectric layers. Mobilities are shown for the backward direction of measurement, as their values are higher than for the forward direction.

Finally, we assessed the optoelectronic performance of both oligomers, namely, electroluminescence and photoelectric effect in OFETs. Though the fabricated OFETs were unipolar, with the only one type of charge carriers are present in the channel (electrons), light emission is suggested to originate from charge recombination at (or near) the interface between the organic semiconductor and the electrode (source or drain), which injects the minor charge carriers (holes).[64] Similarly the photoelectric effect in such devices can occur near the one electrode.[65] Electroluminescence was observed in OFETs based on both oligomers and its intensity was 2.5 times higher in the N-substituted oligomer. OFET images taken during the current characteristics measurements and other details are given in Fig. S13.† For both oligomers, a comparable photoelectric effect was observed so that the drain current exhibited an enhancement up to ~30% depending on V_G under illumination by a white LED (Fig. S14†). In summary, the thin-film OFETs based on the two oligomers showed comparable charge-transport properties, electroluminescence intensity, and photoelectric effect.

3.4. Comparison of N-substitution and fluorination of thiophene–phenylene co-oligomers

It is instructive to compare the impact of the N-substitution on various properties of **CF_3-PTTP-CF_3** with the effect of fluorination on the properties of the another thiophene–phenylene co-oligomer PTPTP (P and T stand for phenyl(ene) and thiophene, respectively), which was recently reported in ref. 16. Both series of oligomers have been investigated as active layers of OFETs and OLETs and have shown promising characteristics. In both cases, electronegative atoms (N or F) are introduced into the molecule resulting in a dramatic change of the electrostatic potential (see Fig. 2(e–f) and ref. 16). The difference between the fluorination and N-substitution is that in the former case, peripherical atoms that are not significantly involved into the π-conjugation are substituted, while in the latter case, the very interior of the conjugated core is altered. In the following, we briefly compare the impact of the two substitution strategies on the HOMO/LUMO energies, optical properties, Raman spectra, crystal structure, and electron transport.

Both type of substitution resulted in planarization of the molecules induced by the elimination of the repulsion of the hydrogen atoms from the adjacent thiophene and phenyl(ene) rings. Introduction of 4, 10, and 14 fluorine atoms into the PTPTP molecule resulted in the decrease of its theoretical HOMO (LUMO) by 0.2 (0.35), 0.4 (0.5) and 0.6 (0.8) eV, correspondingly. Similarly, the N-substitution *via* replacement of just two N atoms in **CF_3-PTTP-CF_3** resulted in the decrease of theoretical HOMO (LUMO) by 0.4 (0.4) eV. The stronger effect of the N-substitution can be attributed to the higher π-electron density at the substituted atoms as mentioned in Section 3.1.1. The optical properties also varied in a similar way: both the F- and N-substitution resulted in the blueshift of absorption and emission spectra (see Fig. 8 and ref. 16). The PLQY in diluted solutions did not change significantly with the substitution. The changes of the Raman spectra revealed the difference in the position of substitution: in the PTPTP series, the phenyl(ene)-associated modes are shifted since the phenyl(ene) rings are fluorinated, whereas in the **CF_3-PTTP-CF_3**/**CF_3-PTzTzP-CF_3** pair, the thiophene-associated modes are altered since the thiophene rings were converted into the thiazole ones.

In both series, the substitution resulted in the change of the crystal structure from herringbone motif to π-stacking. This is in line with the widely observed transition to π-stacking as a result of substitution with electronegative atoms (*e.g.* N, F, Cl, *etc.*).[7,15,66–68] For instance, whereas bithiophenes pack in a herringbone motif, bithiazoles pack in a π-stacking manner.[28] The intra-ring N-substitution of oligoacenes also results in the crossover to the π-stacking structure.[69] These changes can be explained by the changes in the molecular electrostatics: the mentioned atoms in the molecular structure bear a negative charge, which attracts positively charged hydrogen and carbon atoms of the adjacent molecules stabilizing the face-to-face and edge-to-edge molecular interaction and hindering C···H contacts, which are dominant in herringbone packings (Fig. 5). As a result, these rings stack preferentially with the non-substituted rings.

The similar changes in the crystal structure for both series—crossover from herringbone packing to π-stacking with substitution—reveal themselves in the similar changes in the LF Raman spectra, which are very sensitive to the molecular interactions.[47,56,57] Specifically, the LF Raman spectra in both **CF_3-PTzTzP-CF_3** and fluorinated PTPTP ($P_FTP_FTP_F$, P_F stands for fluorinated phenyl(ene)) have much lower intensity (relative to the high-frequency part) than that in **CF_3-PTTP-CF_3** and PTPTP (see Fig. S8†). Since the Raman intensity is associated with vibrational modulation of the material polarizability,[47,70,71] a decrease of the LF Raman intensity can be attributed to a weaker impact of the corresponding vibrations on the charge-transfer integrals between the molecules and intramolecular charge delocalization, which determine the OSs polarizability. This decrease is expected to be favorable for charge transport.[46,47,59,60] Thus, the fluorination and N-substitution not just increase the charge-transfer integrals but also inhibit their vibrational modulation.

The abovementioned similar changes in the crystal structure also result in similar changes in the electron transport pathways. Specifically, in both **CF_3-PTTP-CF_3** and PTPTP crystals, electron transfer integrals are large only in one direction – where the molecules are arranged in a parallel manner. On the contrary, in the crystals of **CF_3-PTzTzP-CF_3** and fluorinated PTPTP (P_FTPTP_F, and $P_FTP_FTP_F$) these integrals are considerable in two directions. As a result, the charge transport changes from quasi-one-dimensional to quasi-two-dimensional, which can increase the charge mobility and make it less susceptible to defects.[45] Whether the increase of the charge transport dimensionality is a general effect of electronegative substitution is a subject of further studies.

4. Conclusions

We addressed computationally and experimentally the impact of substitution of two C–H atom pairs with N atoms in the

thiophene ring of a thiophene–phenylene co-oligomer on its properties. The crossover from the herringbone packing motif to π-stacking as a result of N-substitution was explained by the changes in the molecular electrostatic potential and formation of strongly electronegative areas. The Raman spectra indicated the frequency shift for the high-frequency vibrational modes with dominant contribution from the motion of thiophene/thiazole rings, while the modes associated mostly with phenylene rings vibrations were nearly unaffected. The low-frequency part of the Raman spectra was suppressed with the N-substitution, which can be attributed to the suppression of thermal fluctuation of the charge-transfer integrals. The theoretical charge mobility for N-substituted oligomer was found considerably higher than that for unsubstituted one; this was attributed to the large charge transfer integrals in the directions with large distance between the centers of adjacent molecules and decrease in the reorganization energy. Thin films of both oligomers demonstrated in OFET only electron transport with comparable charge-carrier mobilities, electroluminescence intensities, and photoelectric effect. An intriguing similarity between the effects of N-substitution and fluorination of thiophene–phenylene oligomers was revealed, which is probably a part of more general effect of electronegative substitution. The obtained results are anticipated to be an important contribution into the investigation of the structure–property relationships for organic semiconductors that will stimulate the rational design of these materials.

Conflicts of interest

There are no conflicts to declare.

Acknowledgements

Fabrication and studies of OFETs were supported by Russian Science Foundation (project #18-79-00341). Computational study of molecular properties and charge transport, as well as experimental studies of Raman spectra were supported by Russian Science Foundation (project #18-72-10165). Theoretical analysis of the crystal structures was performed with the support from the Foundation for the advancement of theoretical physics and mathematics "BASIS". UV/vis spectroscopy and fluorescence measurements in solution were performed with financial support from the Ministry of Science and Higher Education of the Russian Federation, using the equipment of the Collaborative Access Center "Center for Polymer Research" of ISPM RAS. Experimental Raman and OFET studies were conducted using the equipment purchased under the Lomonosov Moscow State University Program of Development.

References

1 S. Reineke, M. Thomschke, B. Lussem and K. Leo, *Rev. Mod. Phys.*, 2013, **85**, 1245.
2 S. Toffanin, R. Capelli, W. Koopman, G. Generali, S. Cavallini, A. Stefani, D. Saguatti, G. Ruani and M. Muccini, *Laser Photonics Rev.*, 2013, **7**, 1011.
3 A. J. Kuehne and M. C. Gather, *Chem. Rev.*, 2016, **116**, 12823.
4 A. R. Murphy and J. M. Frechet, *Chem. Rev.*, 2007, **107**, 1066.
5 K. J. Baeg, M. Binda, D. Natali, M. Caironi and Y. Y. Noh, *Adv. Mater.*, 2012, **25**, 4267.
6 A. V. Monika, M. K. Tiwari, B. Show and S. Saha, *ACS Omega*, 2020, **5**, 448.
7 Y. Krupskaya, M. Gibertini, N. Marzari and A. F. Morpurgo, *Adv. Mater.*, 2015, **27**, 2453.
8 J. H. Dou, Y. Q. Zheng, Z. F. Yao, Z. A. Yu, T. Lei, X. X. Shen, X. Y. Luo, J. L. Sun, S. D. Zhang, Y. F. Ding, G. C. Han, Y. P. Yi, J. Y. Wang and J. Pei, *J. Am. Chem. Soc.*, 2015, **137**, 15947.
9 B. Milian-Medina and J. Gierschner, *J. Phys. Chem. Lett.*, 2017, **8**, 91.
10 M. Tang and Z. Bao, *Chem. Mater.*, 2011, **23**, 446.
11 H. Adams, J.-L. J. Blanco, G. Chessari, C. A. Hunter, C. M. R. Low, J. M. Sanderson and J. G. Vinter, *Chem.–Eur. J.*, 2001, **7**, 3494.
12 S. Subramanian, S. K. Park, S. R. Parkin, V. Podzorov, T. N. Jackson and J. E. Anthony, *J. Am. Chem. Soc.*, 2008, **130**, 2706.
13 Z.-F. Yao, J.-Y. Wang and J. Pei, *Cryst. Growth Des.*, 2018, **18**, 7.
14 J. Gierschner, M. Ehni, H. J. Egelhaaf, B. Milián Medina, D. Beljonne, H. Benmansour and G. C. Bazan, *J. Chem. Phys.*, 2005, **123**, 144914.
15 M.-H. Yoon, A. Facchetti, C. E. Stern and T. J. Marks, *J. Am. Chem. Soc.*, 2006, **128**, 5792.
16 A. Y. Sosorev, V. A. Trukhanov, D. R. Maslennikov, O. V. Borshchev, R. A. Polyakov, M. S. Skorotetcky, N. M. Surin, M. S. Kazantsev, D. I. Dominskiy, V. A. Tafeenko, S. A. Ponomarenko and D. Y. Paraschuk, *ACS Appl. Mater. Interfaces*, 2020, **12**, 9507.
17 E. A. Komissarova, D. I. Dominskiy, V. E. Zhulanov, G. G. Abashev, A. Siddiqui, S. P. Singh, A. Y. Sosorev and D. Y. Paraschuk, *Phys. Chem. Chem. Phys.*, 2020, **22**, 1665.
18 H. E. Katz, A. J. Lovinger, J. Johnson, C. Kloc, T. Siegrist, W. Li, Y. Y. Lin and A. Dodabalapur, *Nature*, 2000, **404**, 478.
19 A. F. Lv, Y. Li, W. Yue, L. Jiang, H. L. Dong, G. Y. Zhao, Q. Meng, W. Jiang, Y. D. He, Z. B. Li, Z. H. Wang and W. P. Hu, *Chem. Commun.*, 2012, **48**, 5154.
20 A. Y. Sosorev, M. K. Nuraliev, E. V. Feldman, D. R. Maslennikov, O. V. Borshchev, M. S. Skorotetcky, N. M. Surin, M. S. Kazantsev, S. A. Ponomarenko and D. Y. Paraschuk, *Phys. Chem. Chem. Phys.*, 2019, **21**, 11578.
21 Q. Miao, *Adv. Mater.*, 2014, **26**, 5541.
22 Z. X. Liang, Q. Tang, J. B. Xu and Q. A. Miao, *Adv. Mater.*, 2011, **23**, 1535.
23 S. Ando, R. Murakami, J. Nishida, H. Tada, Y. Inoue, S. Tokito and Y. Yamashita, *J. Am. Chem. Soc.*, 2005, **127**, 14996.
24 S. Ando, J. Nishida, H. Tada, Y. Inoue, S. Tokito and Y. Yamashita, *J. Am. Chem. Soc.*, 2005, **127**, 5336.
25 O. Ostroverkhova, *Chem. Rev.*, 2016, **116**, 13279.
26 K. Navamani, G. Saranya, P. Kolandaivel and K. Senthilkumar, *Phys. Chem. Chem. Phys.*, 2013, **15**, 17947.
27 I. Yavuz, S. A. Lopez, J. B. Lin and K. N. Houk, *J. Mater. Chem. C*, 2016, **4**, 11238.

28 M. D. Curtis, J. Cao and J. W. Kampf, *J. Am. Chem. Soc.*, 2004, **126**, 4318.
29 A. Pron, P. Gawrys, M. Zagorska, D. Djurado and R. Demadrille, *Chem. Soc. Rev.*, 2010, **39**, 2577.
30 M. W. Schmidt, K. K. Baldridge, J. A. Boatz, S. T. Elbert, M. S. Gordon, J. H. Jensen, S. Koseki, N. Matsunaga, K. A. Nguyen, S. Su, T. L. Windus, M. Dupuis and J. A. Montgomery, *J. Comput. Chem.*, 1993, **14**, 1347.
31 M. S. Gordon and M. W. Schmidt, *Theory and Applications of Computational Chemistry: the first forty years*, ed. C. E. Dykstra, G. Frenking, K. S. Kim and G. E. Scuseria, Elsevier, Amsterdam, 2005.
32 V. Coropceanu, J. Cornil, D. A. da Silva, Y. Olivier, R. Silbey and J.-L. Brédas, *Chem. Rev.*, 2007, **107**, 926.
33 Y. Li, V. Coropceanu and J.-L. Brédas, *The WSPC Reference on Organic Electronics: Organic Semiconductors*, ed. J.-L. Brédas and S. R. Marder, World Scientific, Singapore, 2016.
34 B. Baumeier, J. Kirkpatrick and D. Andrienko, *Phys. Chem. Chem. Phys.*, 2010, **12**, 11103.
35 J. Kirkpatrick, *Int. J. Quantum Chem.*, 2008, **108**, 51.
36 H. Kobayashi, N. Kobayashi, S. Hosoi, N. Koshitani, D. Murakami, R. Shirasawa, Y. Kudo and D. Hobara, *J. Chem. Phys.*, 2013, **139**, 014707.
37 *Jmol: an open-source Java viewer for chemical structures in 3D*, http://www.jmol.org/.
38 *Chemcraft – graphical software for visualization of quantum chemistry computations*, http://www.chemcraftprog.com.
39 M. J. Turner, J. J. McKinnon, S. K. Wolff, D. J. Grimwood, P. R. Spackman, D. Jayatilaka and M. A. Spackman, *CrystalExplorer17*, 2017, University of Western Australia, http://www.hirshfeldsurface.net.
40 C. F. Mackenzie, P. R. Spackman, D. Jayatilaka and M. A. Spackman, *IUCrJ*, 2017, **4**, 575.
41 V. A. Postnikov, Y. I. Odarchenko, A. V. Iovlev, V. V. Bruevich, A. Y. Pereverzev, L. G. Kudryashova, V. V. Sobornov, L. Vidal, D. Chernyshov, Y. N. Luponosov, O. V. Borshchev, N. M. Surin, S. A. Ponomarenko, D. A. Ivanov and D. Y. Paraschuk, *Cryst. Growth Des.*, 2014, **14**, 1726.
42 E. A. Shumilkina, O. V. Borshchev, S. A. Ponomarenko, N. M. Surin, A. P. Pleshkova and A. M. Muzafarov, *Mendeleev Commun.*, 2007, **17**, 34.
43 G. A. Crosby and J. N. Demas, *J. Phys. Chem.*, 1971, **75**, 991.
44 S. A. Siddiqui, A. Al-Hajry and M. S. Al-Assiri, *Int. J. Quantum Chem.*, 2016, **16**, 339.
45 J. Gierschner and S. Y. Park, *J. Mater. Chem. C*, 2013, **1**, 5818.
46 A. Y. Sosorev, D. R. Maslennikov, O. G. Kharlanov, I. Y. Chernyshov, V. V. Bruevich and D. Y. Paraschuk, *Phys. Status Solidi RRL*, 2019, **13**, 1800485.
47 A. Y. Sosorev, I. Y. Chernyshov, D. Y. Paraschuk and M. V. Vener, in *Molecular Spectroscopy*, ed. Y. Ozaki, M. J. Wójcik and J. Popp, Wiley, 2019, ch. 15, pp. 425–458.
48 S. Ando, J. Nishida, H. Tada, Y. Inoue, S. Tokito and Y. Yamashita, *CCDC 1427491: Experimental Crystal Structure Determination*, 2015, DOI: 10.5517/cc1jxf3z.
49 S. Ando, R. Murakami, J. Nishida, H. Tada, Y. Inoue, S. Tokito and Y. Yamashita, *CCDC 291639: Experimental Crystal Structure Determination*, 2006, DOI: 10.5517/cc9sgq7.
50 M. Y. Chen, L. J. Yan, Y. Zhao, I. Murtaza, H. Meng and W. Huang, *J. Mater. Chem. C*, 2018, **6**, 7416.
51 G. Gryn'ova, K. H. Lin and C. Corminboeuf, *J. Am. Chem. Soc.*, 2018, **140**, 16370.
52 J. J. McKinnon, M. A. Spackman and A. S. Mitchell, *Acta Crystallogr., Sect. B: Struct. Sci.*, 2004, **60**, 627.
53 M. A. Spackman and P. Byrom, *Chem. Phys. Lett.*, 1997, **267**, 215.
54 M. A. Spackman and J. J. McKinnon, *CrystEngComm*, 2002, **4**, 378.
55 A. J. Edwards, C. F. Mackenzie, P. R. Spackman, D. Jayatilaka and M. A. Spackman, *Faraday Discuss.*, 2017, **203**, 93.
56 A. Brillante, I. Bilotti, R. G. Della Valle, E. Venuti and A. Girlando, *CrystEngComm*, 2008, **10**, 937.
57 A. Brillante, I. Bilotti, R. G. Della Valle, E. Venuti, M. Masino and A. Girlando, *Adv. Mater.*, 2005, **17**, 2549.
58 A. Y. Sosorev, D. R. Maslennikov, I. Y. Chernyshov, D. I. Dominskiy, V. V. Bruevich, M. V. Vener and D. Y. Paraschuk, *Phys. Chem. Chem. Phys.*, 2018, **20**, 18912.
59 S. Fratini, D. Mayou and S. Ciuchi, *Adv. Funct. Mater.*, 2016, **26**, 2292.
60 G. Schweicher, Y. Olivier, V. Lemaur and Y. H. Geerts, *Isr. J. Chem.*, 2014, **54**, 595.
61 R. Marcus and N. Sutin, *Biochim. Biophys. Acta*, 1985, **811**, 265–322.
62 A. Y. Sosorev, *Moscow Univ. Phys. Bull.*, 2019, **74**, 639.
63 A. Y. Sosorev, *Phys. Chem. Chem. Phys.*, 2017, **19**, 25478.
64 C.-F. Liu, X. Liu, W.-Y. Lai and W. Huang, *Adv. Mater.*, 2018, **30**, 1802466.
65 K.-J. Baeg, M. Binda, D. Natali, M. Caironi and Y.-Y. Noh, *Adv. Mater.*, 2013, **25**, 4267–4295.
66 E. O. Levina, I. Y. Chernyshov, A. P. Voronin, L. N. Alekseiko, A. I. Stash and M. V. Vener, *RSC Adv.*, 2019, **9**, 12520.
67 X. P. Cui, C. Y. Xiao, W. Jiang and Z. H. Wang, *Chem.–Asian J.*, 2019, **14**, 1443.
68 S. E. Koh, B. Delley, J. E. Medvedeva, A. Facchetti, A. J. Freeman, T. J. Marks and M. A. Ratner, *J. Phys. Chem. B*, 2006, **110**, 24361.
69 K. E. Maly, *Cryst. Growth Des.*, 2011, **11**, 5628.
70 C. Ambrosch-Draxl, H. Auer, R. Kouba, E. Y. Sherman, P. Knoll and M. Mayer, *Phys. Rev. B: Condens. Matter Mater. Phys.*, 2002, **65**, 064501.
71 R. Scholz, L. Gisslén, C. Himcinschi, I. Vragović, E. M. Calzado, E. Louis, E. S. Maroto and M. A. Díaz-García, *J. Phys. Chem. A*, 2009, **113**, 315.